Available online at www.sciencedirect.com

jmr&t Journal of Materials Research and Technology

journal homepage: www.elsevier.com/locate/jmrt

Original Article

Effect of the crucible composition on the Inconel 718 vacuum induction melting process efficiency

Pablo Garcia-Michelena [a,*], *Xabier Chamorro* [a], *Nuria Herrero-Dorca* [a], *Daniel Bernal* [a], *Iñaki Hurtado* [a], *Emilio Ruiz-Reina* [b], *Jesus Mariano Arnesto* [c], *Oscar Caballero* [c], *Xabier Esquisabel* [c], *Iñaki Madariaga* [d]

[a] *Mechanical and Manufacturing Department, Mondragon University, Mondragon, 20500, Spain*
[b] *Institute Carlos I for Theoretical and Computational Physics (iC1), Departamento de Física Aplicada II, Universidad de Málaga, Málaga, 29071, Spain*
[c] *Technology Department, ITP Aero Castings, Barakaldo, 48901, Spain*
[d] *Materials and Processes Department, ITP Aero, Zamudio, 48170, Spain*

ARTICLE INFO

Article history:
Received 7 December 2022
Accepted 29 January 2023
Available online 6 February 2023

Keywords:
Vacuum induction melting
Inconel 718
Thermal characterization
Crucible
Casting optimization

ABSTRACT

Nickel-based superalloys are widely employed to manufacture aero-engine turbines due to their high mechanical strength and resistance to corrosion and creep. Vacuum Induction Melting (VIM) is a suitable manufacturing technology because of the reactive nature of the alloying elements; however, the melting process is time-consuming and energy-demanding. This research focuses on increasing the overall efficiency of the process in two ways. Initially, studying the influence of metal-containing crucible composition and thermal properties on the melting. In a semi-industrial VIM facility, 2 kg of Inconel 718 alloy was melted employing Al_2O_3, ZrO_2, MgO, and $Al_6Si_4O_{13}$-based crucibles. The $Al_6Si_4O_{13}$ and ZrO_2-based crucibles reduced energy consumption by 28% and 23%, respectively, compared to the reference crucible of Al_2O_3. Subsequently, an optimized melting procedure is proposed to reduce the process cycle time and energy demand, saving 10%–20% for all crucibles compared to the standard melting procedure. In addition, the ZrO_2 and $Al_6Si_4O_{13}$ crucibles reduced total cycle time by 13% and 21%, respectively. During melting, intense dross formation was detected for all crucibles, dissipating faster for $Al_6Si_4O_{13}$ and MgO crucibles. Therefore, the metal-crucible interface product was analyzed to understand these mechanisms better, and the four crucibles' chemical reactivity was examined.

* Corresponding author.
E-mail address: pgarciam@mondragon.edu (P. Garcia-Michelena).

https://doi.org/10.1016/j.jmrt.2023.01.213

1. Introduction

Nickel-based superalloys are critical materials for the aeronautical industry due to their exceptional properties: high strength, fatigue, creep, and resistance to oxidation at high operating temperatures [1]. These properties result from a complex microstructure, precipitation of the γ' and γ'' phase [2], and the presence of carbides obtained from a precise alloy composition, solidification conditions, and heat treatments [3]. Turbine and compressor components such as blades and vanes have complex geometries, curvatures, sharp corners, and thin walls [4]. For this reason, investment casting is considered the most suitable near-net shape manufacturing process due to its flexibility and limited material wastage [5]. Specific melting techniques to obtain an impurity-free melt, such as Vacuum Induction Melting (VIM), are required to ensure a non-reactive atmosphere and precise alloy composition before pouring [6].

Like other metal melting technologies, VIM is a time-consuming and energy-demanding process. Baake et al. [7] state that the electrical efficiency ranges between 50% and 70% for non-ferrous alloys. Previous works on optimization have mainly analyzed the electromagnetic aspects of the process by enhancing the coil-to-charge coupling [8] and minimizing power generator losses via optimum resonant power converter design [9]. Related to the VIM process parameters, Fleming et al. [10] related the induced heating power and melt superheat temperature [11] with the oxygen and nitrogen content and subsequent microstructural and physical properties of investment cast ASTM F75 alloy.

In many cases, optimization is accompanied by the development of numerical models, which reduces costs and increases flexibility. The principal investigations into induction melting have considered electromagnetic stirring of the melt and its turbulence behavior [12], melt free surface dynamics [13], and particle transport models [14]. Bulinski et al. [15] developed and validated a numerical model considering the free surface deformation and top surface temperature transition for aluminum melt. However, no experimental data on VIM technology for nickel-based superalloys correlates with the developed models.

The influence of other critical melting process elements, such as the crucible essential to contain the melt, has not been considered for the efficiency of the process. The crucibles and liners employed in VIM facilities are made of ceramic materials, which provide high thermal resistivity and chemical stability [16]. To date, literature on crucibles for nickel-based superalloys has focused on physical erosion [17] and the chemical interaction between the crucible and melt [18]. Gao et al. [19] analyzed the reaction mechanism of VIM melting in Al_2O_3, MgO, and MgO-Spinel crucibles. The authors concluded that for Al_2O_3 physical erosion is dominant, whereas dissolution and chemical reactions are dominant for the last crucibles. Valenza et al. [20] also studied the superficial wetting and the interaction between nickel-based superalloys and various ceramic materials, concluding that Al, Zr, and Hf form interface compounds.

Regarding thermal aspects, heat transfer of refractories has been of particular interest during metal solidification into molds [21]; however, the influence on crucibles and liners during the melting process has not yet been studied. The thermal properties of the crucibles play an essential role, as there is heat conduction from the melt to the surroundings through the crucible. Principal physical variables that determine thermal conductivity are bulk density, phase composition, microstructure, and humidity [22]. Even though there are reference values in databases and handbooks, considerable scattering has been found, limited to specific compositions, relatively low measuring temperatures, and without a unified criterion for measuring techniques [23]. Vitiello et al. [24] compared the thermal conductivity characterization with four techniques for vermiculite and clay-based refractories, concluding that sample humidity, porosity, and heterogeneity induce a minimum discrepancy of 10% in the measurement. Schultz et al. [25] characterized the thermal conductivity of Al_2O_3-spinel and MgO-spinel compounds, concluding that lower conductivity was obtained at higher spinel volume fractions. Shi and Pinto. [26] developed finite element models based on the thermal properties of crucibles to study the energy consumption and efficiency during the melting and holding of aluminum. Related to modeling, Akiyoshi et al. [27] developed precise, statistical models capable of estimating the thermal conductivity of refractories depending on the temperature or porosity, concluding that accuracy decays when the dependent physical variables are increased. Thus, correctly characterizing the crucible materials' thermal properties is crucial to understanding the different phenomena that affect the melting stage.

Therefore, the scope of this study is threefold: (i) analyze the effect of the ceramic crucible thermal properties on the efficiency of the VIM process. (ii) Optimize the melting procedure of the nickel-based Inconel 718 superalloy to save energy and process time (iii) measure the possible reaction products in the metal-crucible interface.

2. Materials and methods

2.1. *VIM facility*

A semi-industrial VIM facility (Fig. 1) manufactured by SECO-Warwick S.A. (Świebodzin, Poland) with a capacity to melt 2 kg of Inconel 718 was employed for the melting trials. The hot crucible melt-box has a seven-turn coil connected to a 100 kW 10 kHz solid-state converter power unit. Inside the coil, a crucible was introduced, employing a new one for each trial. A magnesia ramming layer was added as a second protection layer between the crucible and coil. The vacuum level achieved inside the chamber is in the order of 0.1 Pa. During operation, a constant argon flow of 1 Pa is top added to prevent alloy oxidation with the remaining atmosphere due to the higher density of the argon. The vacuum level was maintained in the same order of magnitude for all trials and crucibles.

Real-time process parameters were recorded during melting. The energy applied during the test is obtained directly from the data of the power generator itself. An Optris CTRatio_1 MH dual-wavelength pyrometer that automatically corrects emissivity changes was employed to measure the top surface temperature of the metal. The pyrometer has a

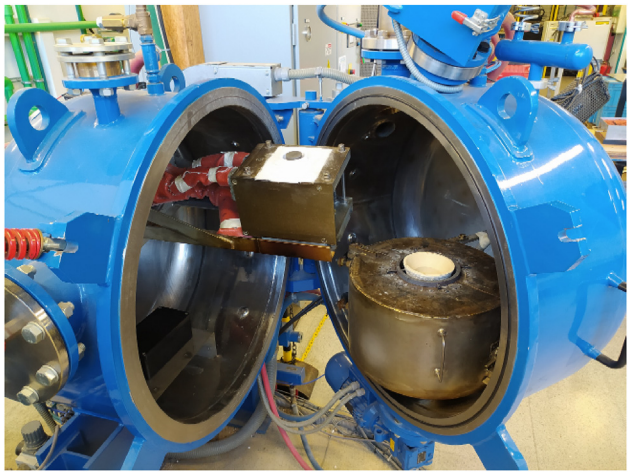

Fig. 1 – VIM facility, vacuum chamber, and hot crucible melt-box detail.

measuring range between 700 °C and 1800 °C and was placed outside the vacuum chamber aiming from a viewport. A calorimetric flow sensor displayed the water flow of the melt box, and two resistance temperature detectors were installed for the inlet and outlet water temperature. A four-channel universal analog input module, NI 9207, was used to acquire data from each sensor at 1 Hz.

2.2. *Material selection*

The melted material was the nickel-based superalloy Inconel 718, widely employed in the aeronautic sector. Cast bars produced by Cannon-Muskegon Corp. (Muskegon, MI, USA) with dimensions of Ø 45 mm, 160 mm height, and a weight of 2 kg were employed for the tests. Before the melting test, a differential scanning calorimetric (DSC) analysis was performed on a sample of the ingots using a Netzsch STA 449 F3 Jupiter®. The analysis identified the phase transition temperatures with 1260 °C for solidus and 1359 °C for liquidus. An overheating of 90 °C was set, fixing 1450 °C as the target pouring temperature in the casting trials.

Commercial isostatically pressed refractory crucibles manufactured by Capital Refractories LDT (Clowne, Chesterfield, U.K.) were selected for the casting trials based on alumina (AL97I), magnesia (MG95I), mullite (ML72I), and zirconia (ZC93I). For the performance comparison, AL97I was considered the reference crucible material as it is widely employed in the industry. All testing crucibles had the exact final dimensions, inner Ø 62 mm and 160 mm height and outer Ø 75 mm and 175 mm height. The chemical composition and phases of crucibles were measured (Table 1), assuming that all the elements are oxides. Wavelength dispersive -X-ray fluorescence (WD-XRF) analysis was done using a PANalytical Axios® model and X-ray diffraction (XRD) with PANalytical Xpert PRO®. The obtained results are in line with the ones facilitated by the crucible manufacturer.

2.3. *Crucible thermal characterization*

The thermal conductivity (Fig. 2a) was characterized as the product of the density, thermal diffusivity, and specific heat capacity $k(T) = \rho \cdot \alpha(T) \cdot Cp(T)$. For each crucible, three samples were tested. Assuming that refractories have a low thermal expansion coefficient, a constant bulk density was determined by the relation of volume and mass. Employing laser flash analysis technique (Linseis LFA 1000®), thermal diffusivity was measured and DSC with sapphire method (Netzsch STA 449 F3 Jupiter®) for specific heat capacity (Fig. 2b).

The obtained results represent the mean value and the standard deviation. The scattering at higher measuring temperatures is related to a reduction of equipment sensitivity at higher temperatures. MG95I and AL97I-based crucibles have a higher specific heat capacity and thermal conductivity. ML72I shows a more linear performance maintaining properties constant even at higher temperatures. On the contrary, ZC93I has the lowest heat capacity increasing once it surpasses the 1000 °C barrier; this could be related to the structure change from monoclinic to tetragonal at 1170 °C, even though thermal conductivity maintains almost constant in all the measurement ranges.

2.4. *Inconel 718 melting procedure*

A standardized melting procedure was established based on the DSC results and the industrial criteria for Inconel 718 melting. This procedure was divided into five stages.

1. A 1-h bake-out stage was included to progressively increase the melt-box and crucible temperature to approximately half the melt temperature. This way, the thermal shock risk was reduced, and the humidity from the crucible was eliminated.
2. After stabilization, a second heating step was applied to increase the charge temperature.
3. In the melting stage, the power was again incremented to accelerate the melting of the entire charge in the shortest possible time. During this stage, dross particles were

Table 1 – Crucible chemical composition measured by WD-XRF.

Crucible Reference	Chemical Analysis [w.t. %]						
	Al_2O_3	SiO_2	MgO	CaO	Fe_2O_3	ZrO_2+HfO_2	Other
AL97I	94.4	4.4	–	0.2	0.5	–	0.5
MG95I	1.1	2.1	92.4	2.3	1.1	–	1.0
ML72I	71.0	24.3	–	1.4	1.1	–	2.2
ZC93I	1.7	1.2	–	4.5	0.4	91.0	1.2

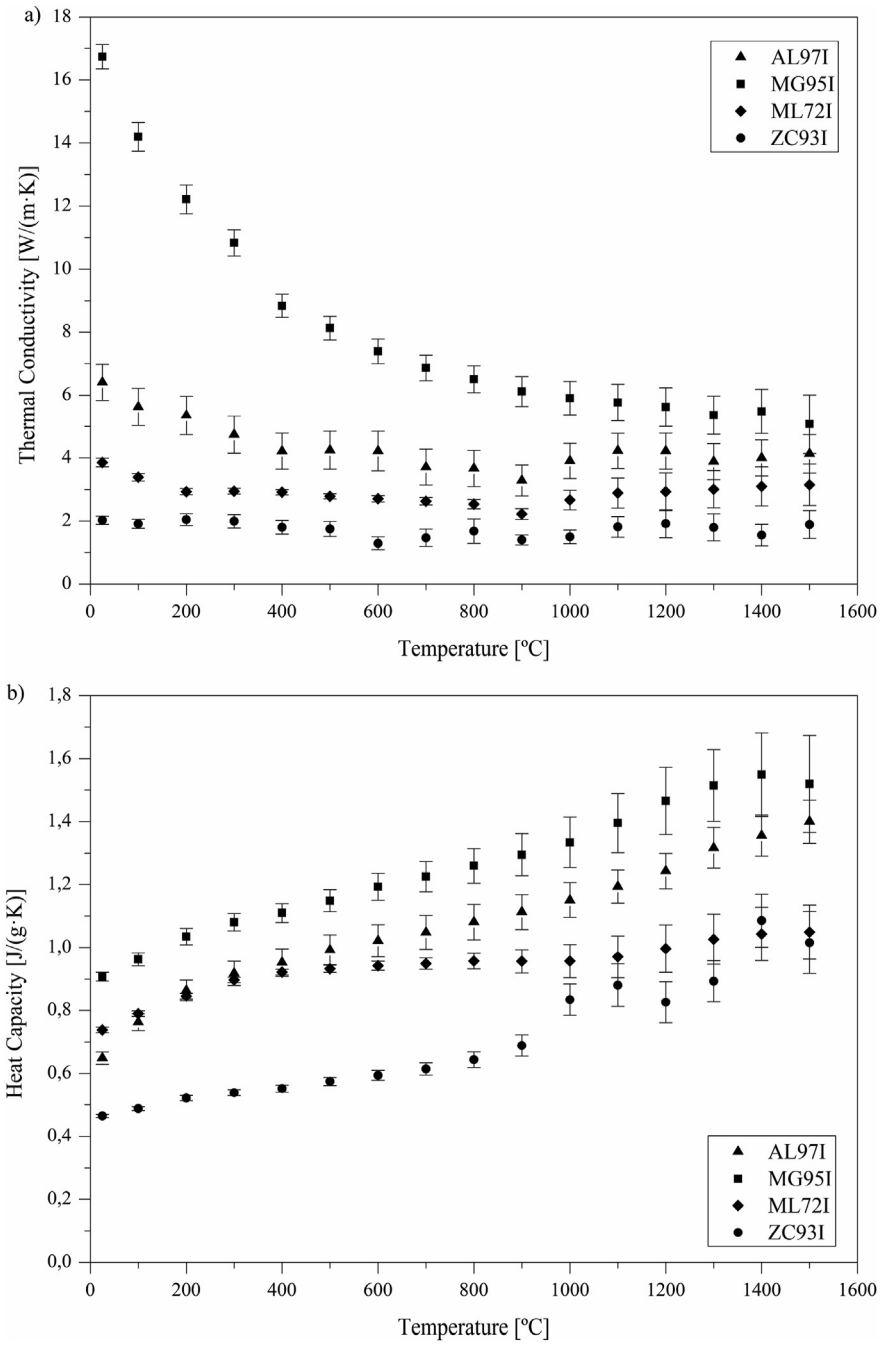

Fig. 2 – Characterization of crucibles' thermal properties. (a) Thermal conductivity. (b) Heat capacity.

detected in all crucibles. They increased progressively and coalescence until a compact layer was formed on the surface of the molten metal (Fig. 3). This phenomenon can be observed in the melting comparison included as multimedia content (MeltingComparison.mp4).

4. In stage 4, the melt temperature was increased to 1500 °C, at which particles started to separate. The temperature was maintained, letting the metal stir until the surface was clear. The time required for clearing varied for each trial. The temperature was manually adapted due to the low thermal inertia of the melt, regulating the applied power with smooth transitions of 0.1 kW. A variability of ±5 °C concerning the objective temperature was achieved during stationary states.
5. Once the melt was free of dross, the melt temperature was reduced to the casting temperature of 1450 °C and maintained for homogenization before pouring into the mold. The temperature control was done with the same procedure as in the previous stage.

The standardized power-time-temperature profile is summarized in Table 2.

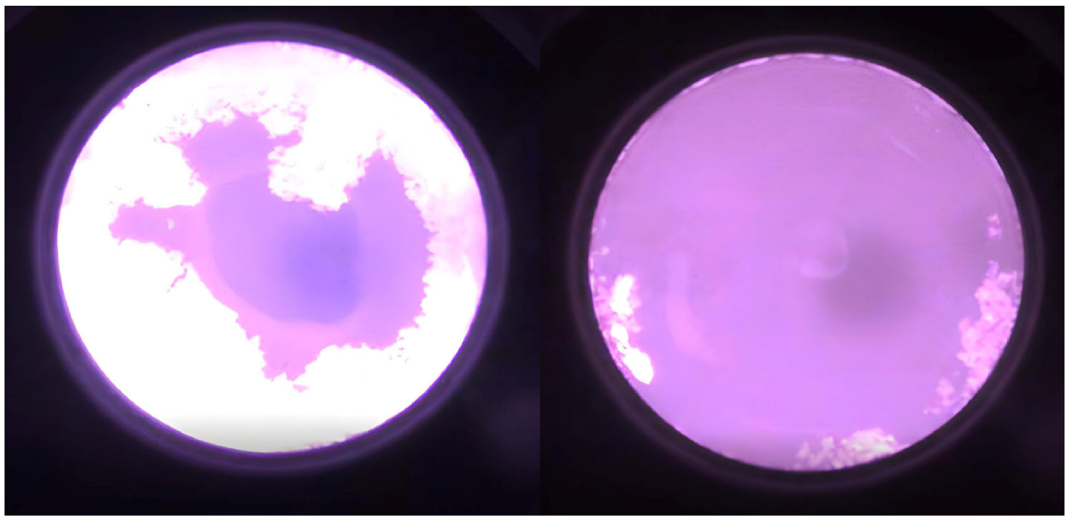

Fig. 3 – Left: Initiation of compact dross separation. Right: Almost the entire surface is cleaned.

Table 2 – Power-time stages for the standardized melting method.

Stage Nº	Description	Power [kW]	Time [min]	Temperature [ºC]
1	Bake-Out	5	60	Variable
2	Heating	11	12	Variable
3	Melting	16	Adaptative	Variable
4	Stirring - Cleaning	Adaptative	15	1500
5	Pouring Temperature	Adaptative	5	1450

3. Results and discussion

3.1. *Standard melting cycle*

Fig. 4 depicts the power-time profile followed from the 60 min bake-out (stage 1) until the pouring of the melt. The AL97I trial, which serves as a reference, determines the duration of the different stages shown in the graph. Power variations in each stage are related to the power adjustments required in each trial and stage to maintain the objective temperatures detailed in 2.4 Inconel 718 Melting Procedure.

It must be highlighted that AL97I and MG95I required 17 kW in stage 3 to melt and reach 1500 °C for the dross cleaning. In addition, it was also necessary to apply higher power to stabilize the melt at 1450 °C in stage 5. The MG95I and the AL97I required similar power, while the ZC93I and ML72I trials needed lower power to reach the same temperature response in all stages.

The evolution of the charge temperature for the four crucibles and the division of stages for the AL97I baseline is plotted in Fig. 5. The magnetic field produces a non-uniform current induction over the charge length, initiating the melting at the base of the cylindrical ingot, which can be viewed in the video recording. This incipient melting displaced the ingot radially. Thus, the sudden temperature variations in the pyrometer between minutes 65 and 85 resulted from the ingot bottom measurement that heated up faster.

The temperature slope of stages 2 and 3 shows different heating gradients for each crucible. The ML72I and ZC93I gradient was stepper, requiring less melting time than the AL97I (8 min less for the ML72I and 5 min for the ZC93I). This is in line with the thermal measurements, where lower heat capacity and thermal conductivity were measured for the last crucibles. Thus it was expected to reduce the heat conduction consequent losses and faster heating. In contrast, the MG95I and AL97I with higher specific heat capacity and conductivity, heating, and melting were displaced in the time axis.

Once the target temperature of 1500 °C was reached, it was maintained during stage 4, adjusting the applied power following thermal inertia. This facilitated dross cleaning while preventing the melt from excessive superheating. During dross-cleaning, it was observed that the particle reduction time was not equal, with the ML72I and MG95I crucibles achieving faster metal cleaning; however, the duration was fixed to 15 min following the standard criteria.

The energy consumption of each trial was evaluated by integrating the total lead time and the power generator supply. Table 3 sets out the energy consumption for the complete melting cycle and compares the energy-saving of each crucible concerning the reference trial AL97I_Std. The MG95I crucible demanded higher energy due to prolonged melting and higher power requirements. In contrast, the ZC93I and ML72I presented faster heating, with the former consuming 23% and the latter 28% less energy than the baseline.

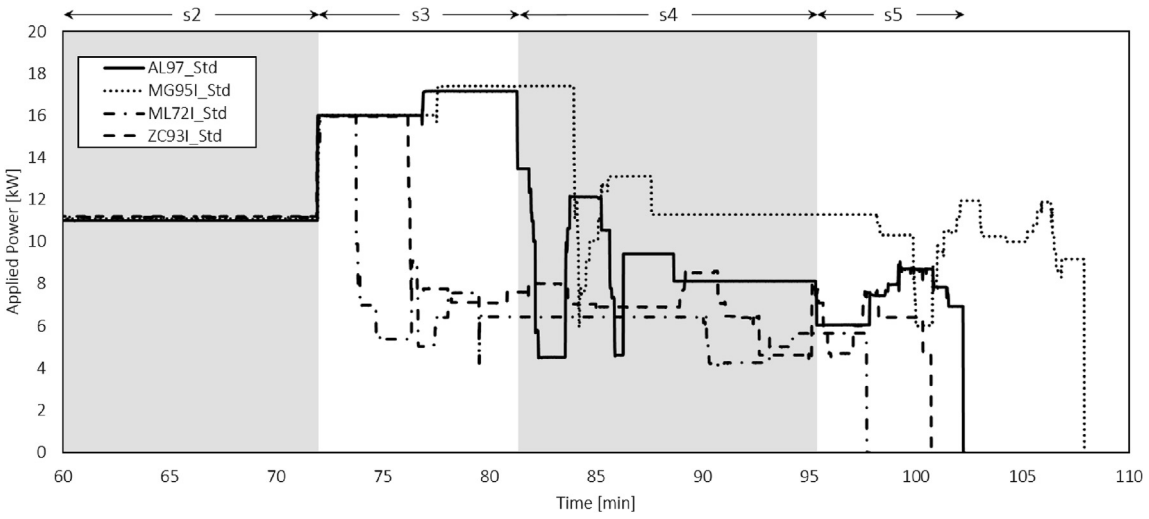

Fig. 4 – Standardized melting procedure, applied power as a function of time for the four crucibles.

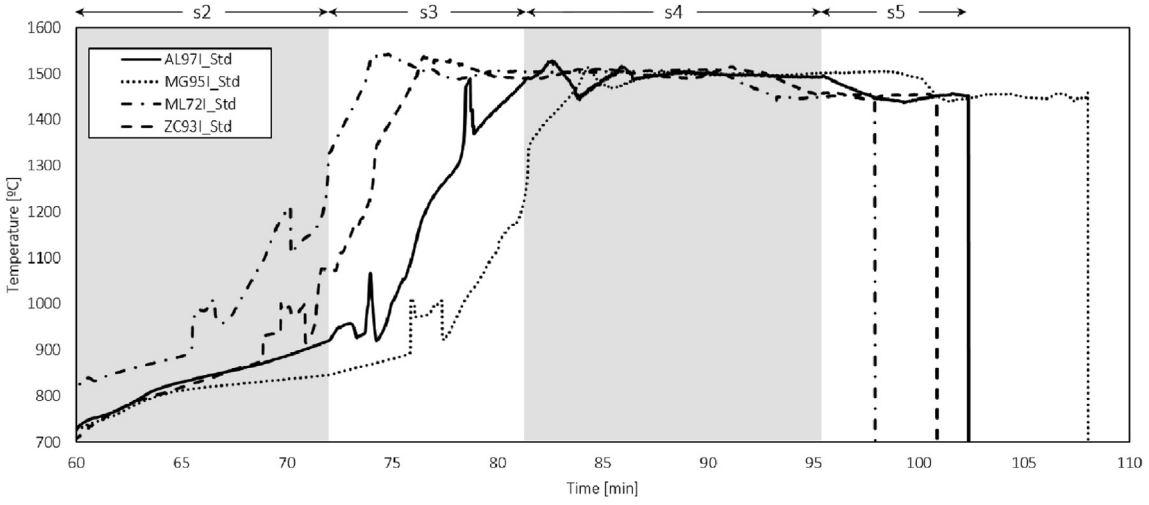

Fig. 5 – Standardized melting procedure, temperature as a function of time for the four crucibles.

Table 3 – Energy consumption for standard melting and crucible comparison.

Melting Trial	Energy Consumption [kJ]	Crucible Comparison [%]
AL97I_Std	846.8	–
MG95I_Std	929.3	+10
ML72I_Std	611.6	- 28
ZC93I_Std	648.7	- 23

3.2. *Optimized melting cycle*

A second trial was performed, optimizing the power profile by minimizing the dross-cleaning time in stage 4 instead of applying a standard fixed duration. Fig. 6 illustrates the power-time graph. The standard criteria was followed until stage 2. In stage 3, the melting time was adapted to the thermal response, and it was confirmed that AL97I and MG95I required the additional step of 17 kW for 4.5 and 6.5 min, respectively. In contrast, a 16 kW step for 2 min for the ML72I and 5 min for the ZC93I was enough to melt the charge. Then, the applied power and time were adjusted based on the temperature evolution of the melt. The objective was to maintain the target temperature while enhancing the dross separation velocity. In this latter, less power and time were required for the ML72I and MG95I.

The temperature response of the melt during temperature conditioning is shown in Fig. 7. The melting comparison multimedia material (MeltingComparison.mp4) shows each crucible's melting and dross-cleaning processes. The comparison in the video starts with an initial joint frame corresponding to the end of the bake-out (stage 1). Once the ZC93I and ML72I were fully molten, the AL97I incipient melting started, while the MG95I required the longest time to melt completely. The dross cleaning time was minimized

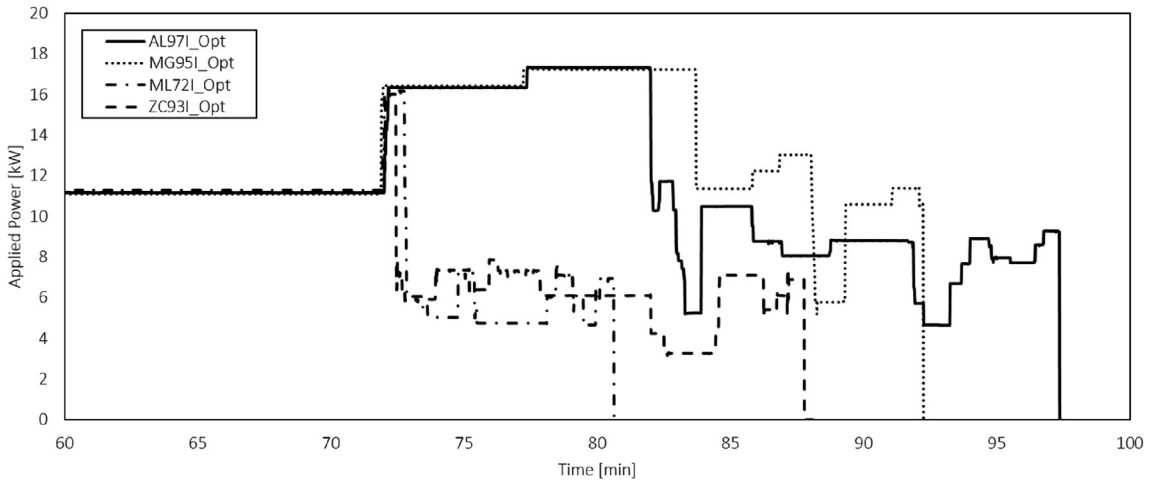

Fig. 6 – Optimized melting procedure, applied power as a function of time for the four crucibles.

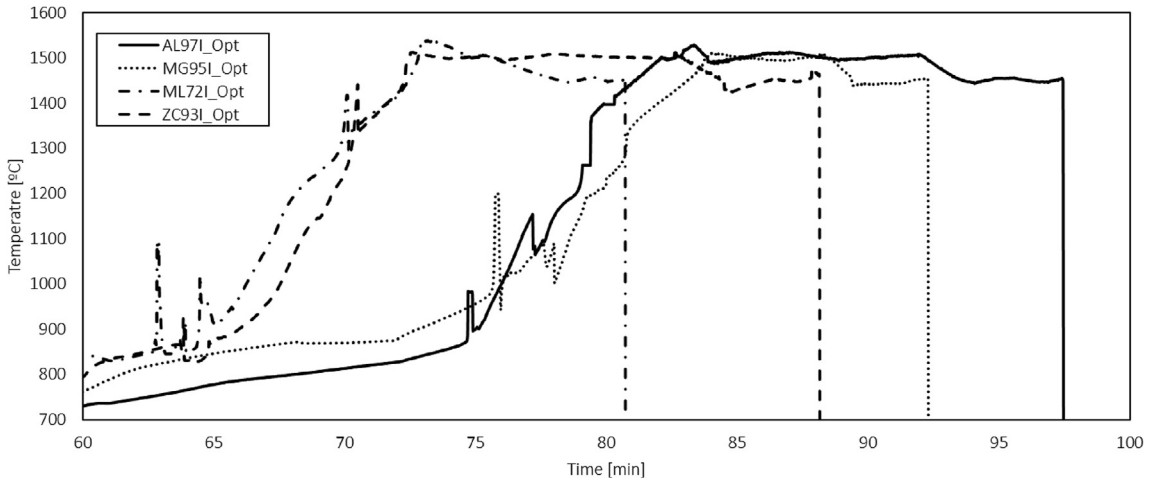

Fig. 7 – Optimized melting procedure, temperature as a function of time for the four crucibles.

based on the dissipation velocity, and the temperature was maintained, which reduced the duration of stage 4. The video identifies the dross cleaning times, summarized in Table 4. After the melt top surface was clean, the power was reduced to decrease the temperature in stage 5 and then maintained for 5 min for homogenization before metal pouring.

The lead time saving for the optimized melting was analyzed by evaluating three critical intervals and compared to the AL97I_Opt (Table 4). The ZC93I and ML72I crucibles required 24% and 45% less time for the melting and dross cleaning steps than the AL97I. Again it is confirmed that melting time is directly related to thermal properties. The AL97I and MG95I melting trials had a similar total duration except for the dross cleaning, stage 4, where ML72I and MG95I were the crucibles that presented a faster dross cleaning.

The thermal properties alone cannot justify why the MG95I could be faster than the ZC93I, as MG95I is the crucible with higher thermal conductivity. Thus, it is necessary to open the scope to additional aspects, such as the analysis of the dross's nature and formation and interaction with the crucible, to understand the dross-cleaning mechanisms.

Table 4 – Detailed interval comparison between crucibles.

Evaluated interval	Stages	Duration [min]			
		AL97I_Opt	MG95I_Opt	ML72I_Opt	ZC93I_Opt
Melting time	2–3	20	22	11	11
Dross cleaning	4	13	7	5	12
Cycle time	2–5	38	34	21	28

Table 5 – Energy saving by procedure comparison for tested crucibles.

Crucible Reference	Energy Consumption [kJ]		Procedure Comparison [%]
	Standard	Optimized	
AL97I	846.8	755.8	- 11
MG95I	929.3	733.1	- 21
ML72I	611.6	485.6	- 21
ZC93I	648.7	528.2	- 19

Table 6 – Cycle time by procedure comparison for tested crucibles.

Crucible Reference	Cycle Time [min]		Procedure Comparison [%]
	Standard	Optimized	
AL97I	102	98	- 4
MG95I	108	93	- 14
ML72I	98	81	- 17
ZC93I	102	89	- 13

3.3. *Melting procedure comparison*

In Table 5, the optimized melting cycle of each crucible is compared to the previously discussed standard melting profile, revealing energy savings of between 10% and 20% for each. Evaluating the optimized melting trials with AL97I_Std baseline, reductions in energy consumption of 43% for the ML72I_Opt and 38% for the ZC93I_Opt were obtained.

Similarly, a cycle time reduction following the optimized melting procedure is achieved for all crucibles (Table 6). Moreover, the lead time was reduced by 13% and 21% for ZC93I_Opt and ML72I_Opt, respectively, compared to the AL97I_Std baseline.

3.4. *Dross composition analysis*

Focusing on dross cleaning, the thermal conductivity of crucibles is not the unique factor to explain the different behavior. After pouring, all crucibles were examined without finding any evidence of isolated dross particles. However, solidified metal layers were found attached to the crucible's inner walls. In a visual analysis, ceramic remains were observed, which could contain particles and possible reaction products of the interaction between the metal-crucible.

First, a local semi-quantitative chemical composition analysis of the detached layers was done employing scanning electron microscopy (SEM) and energy-dispersive X-ray spectroscopy (EDS) with a Fei Nova Nanosem 450®. A section of the sample (Fig. 8) corresponding to the interphase between dross and crucible was analyzed for all crucibles. MG95I_Opt crucible was selected as a representative case, the fastest for the dross cleaning stage. The measured local points are identified, and the elemental composition results are summarized in Table 7.

The main matrix composition corresponding to Point 1 is rich in Mg, O, and Al— the product of the possible reaction. In addition, several Al, Ti, and Nb-rich compounds were detected in Points 2 and 3. These metallic oxides have been detected for all crucibles in different proportions, thus, indicating the possible composition of the dross particles. The presence of complex metallic oxides together with Mg may be due to the formation of a thinner slag during melting as a consequence of the oxidation process in the MgO-based crucible.

3.5. *Crucible reactivity*

Tested crucibles were examined to find evidence of the melt-to-crucible reaction and the formation of new compounds. Samples from the crucibles that were in contact with the molten metal were extracted and grounded for WD-XRF and XRD inspection. As received, new crucible samples were also examined for reference. The Al97I, ZC93I, and ML72I samples did not contain any relevant quantity of reaction products, while MG95I produced compounds are presented in the XRD spectrum of Fig. 9.

Analysis reveals the presence of $MgAl_2O_4$ (spinel) as the main crystalline reaction product. Traces of Al_2O_3 (corundum) were also detected. According to the Ellingham

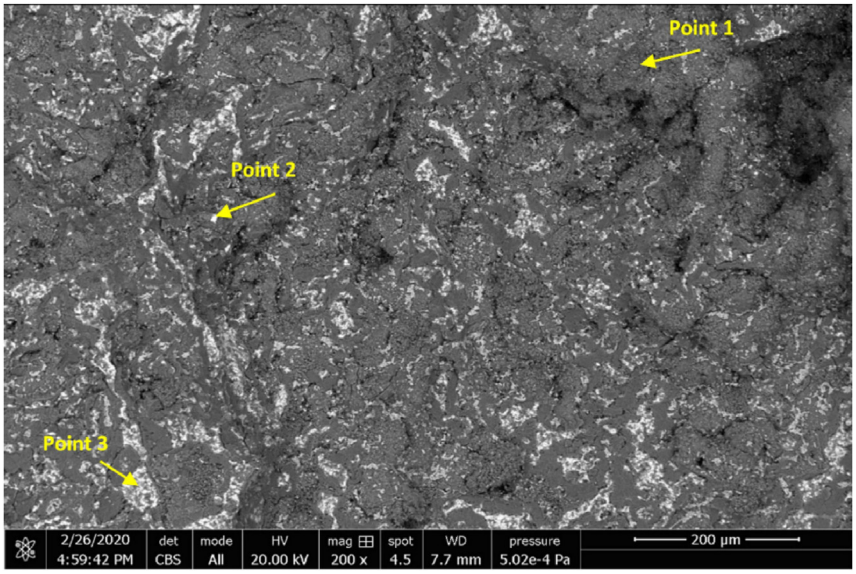

Fig. 8 – BSE image of the dross-crucible face sample. EDS of oxidation products and measured points.

Table 7 – Semi-quantitative chemical composition of detected oxides for MG95I_Opt crucible.

	Chemical Composition, [at.%] Spectrum								
	Ni	Cr	Fe	Nb	Mo	Mg	Ti	Al	O
Point 1	–	3.5	–	–	–	16.7	1.5	37.6	43.7
Point 2	37.7	13.6	12.3	17.6	2.7	4.2	2.4	9.5	–
Point 3	40.1	16.6	15.1	2.7	1.7	–	1.0	22.7	–
Inconel 718	52.5	19	Bal.	5	3	–	0.9	0.6	–

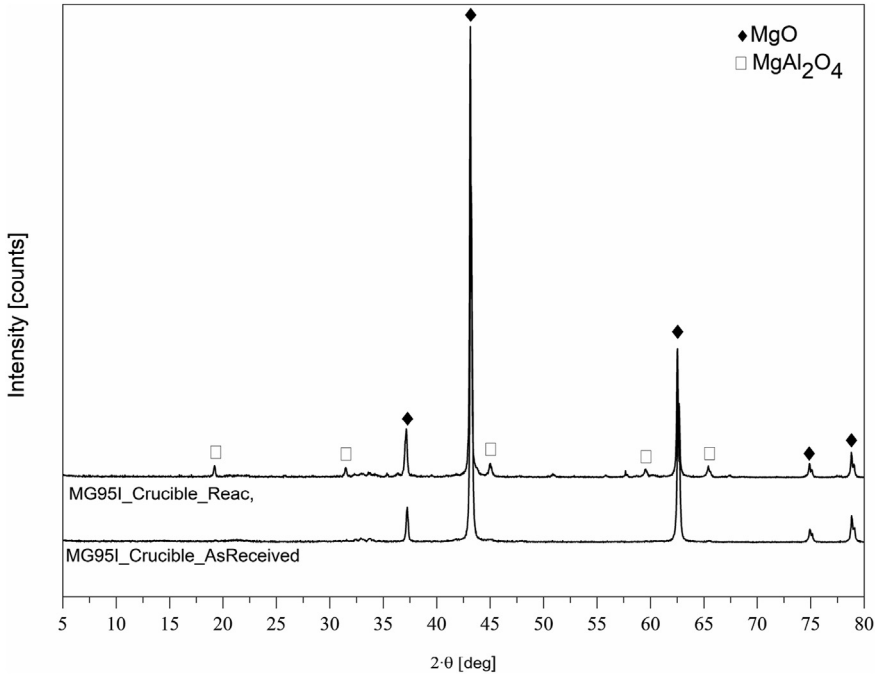

Fig. 9 – Superposition of as received and reacted MG95I crucible samples XRD diffractograms.

diagrams, at 1500 °C, $MgAl_2O_4$ is more stable than MgO or Al_2O_3 [28]. The $MgAl_2O_4$ was likely formed from the reaction between MgO present in the crucible and Al from the alloy. This reaction could be either a direct MgO – metallic Al reaction or/and a MgO–Al_2O_3 reaction previously described by Gao et al. [19]. They evidenced a two-stage reaction for the MgO and MgO-spinel crucibles, where the first Al_2O_3 layer was produced due to the reaction between the MgO crucible and Al of the alloy. In a secondary stage, Al_2O_3 reacted with the MgO of the crucible, deriving it into $MgAl_2O_4$. In parallel, the dissolved Mg from the first stage reduces the Al_2O_3 and Ti_2O_3 inclusions modifying the composition into stable Al–Mg oxides.

Therefore, it is reasonable to assume that MgO–Al_2O_3 reactions may occur since this would also correlate with the presence of Al_2O_3 in the diffractogram. Oxidation of the Al alloying element may be formed after the first reaction of metallic Al with crucible oxides; however, reactions between Al and free O present in the porous ceramic structures or the atmosphere cannot be discounted. The EDS analysis of the dross evidences the presence of Al-oxides, indicating that this Al can only come from the alloy itself and not from the crucible and a possible loss of alloying elements in the melt. Similarly, the detected Mg-rich and Al–Ti oxides could be related to the formation of inclusions.

4. Conclusions

The presented results demonstrate the importance of crucibles on the overall efficiency of the VIM process for the Inconel 718 superalloy. Remarkable energy consumption saving was achieved by only varying the composition of the crucibles. Another benefit was reducing the process cycle time, which was also enhanced by optimizing the melting procedure by minimizing the dross cleaning time. These results can directly impact industrial-scale production facilities contributing to more efficient induction melting practices. Along the same line, consideration of the final thermal properties of crucibles for the future development of new compositions.

- The crucibles' thermal conductivity and heat capacity play a critical role in the heat transfer dynamics between melt and crucible. As expected from the measurements, for lower measured values, faster melting was achieved, as is the case of ML72I and ZC93I crucibles. The optimized melting procedure confirmed the first results and increased energy saving.

However, for the dross cleaning step, the faster performance of MG95I is not possible to explain only with the crucible thermal properties.

- It is not clear the mechanism behind the formation and separation of the dross. For all crucibles, the EDS analysis of the reaction products indicates the formation of Al, Ti, Mg, and Nb oxides. The composition was equal for all crucibles, varying in quantity, indicating the possible composition of the dross particles. Also, it is possible that while the melt depletes alloying elements, the crucible provides free O for forming Al–Mg–Ti oxides.

- All crucibles except MG95I remained chemically stable during melting. Spinel formation in MG95I indicates that aluminum can only come from the alloy itself and not from the crucible.

The summarized power, temperature, and time data can serve as a reference for the experimental validation of numerical models that simulate the VIM melting process currently in development. Further research is necessary to thoroughly understand the effect of chemical composition on the thermal properties of crucibles, the measurement of the heat transfer process, and the mechanisms behind the formation and dissipation of the dross.

Declaration of competing interest

The authors declare that they have no known competing financial interests or personal relationships that might have appeared to influence the work reported in this article.

Acknowledgments

The authors would like to sincerely thank the Basque Government and the Department of Education, Universities, and Research for its financial support by means of the Hazitek FAKTORIA project (ZE-2020/00001) program of the RVCTI.

Appendix A. Supplementary data

Supplementary data to this article can be found online at https://doi.org/10.1016/j.jmrt.2023.01.213.

REFERENCES

[1] Pollock TM, Tin S. Nickel-based superalloys for advanced turbine engines: chemistry, microstructure, and properties. J Propul Power 2006;22:361–74.
[2] Li Y, Dong Y, Jiang Z, Yao K, Du S, Liu Y, et al. Study on microsegregation and homogenization process of a novel nickel-based wrought superalloy. J Mater Res Technol 2022;19:3366–79.
[3] Cui H, Tan Y, Bai R, Li Y, Zhao L, Zhuang X, et al. Effect of melt superheat treatment on solidification behavior and microstructure of new Ni–Co based superalloy. J Mater Res Technol 2021;15:4970–80.
[4] Lagow BW. Materials selection in gas turbine engine design and the role of low thermal expansion materials. JOM 2016;68:2770.
[5] Szeliga D. Manufacturing of thin-walled Ni-based superalloy castings using alternative thermal insulating module to control solidification. J Mater Process Technol 2020;278:116503.
[6] Mitchell A. Melting and refining of superalloys and titanium alloys. ISIJ Int 1992;32:557–62. https://doi.org/10.2355/isijinternational.32.557.
[7] Baake E, Nacke B. Introduction and fundamental principles of induction melting. Induction Heat Heat Treat 2014:405–15. https://doi.org/10.31399/ASM.HB.V04C.A0005895.
[8] Dorland P, Van Wyk JD, Stielau OH. On the influence of coil design and electromagnetic configuration on the efficiency of an induction melting furnace. IEEE Trans Ind Appl 2000;36:946–57. https://doi.org/10.1109/28.855946.
[9] Park HP, Jung JH. Load-adaptive modulation of a series-resonant inverter for all-metal induction heating applications. IEEE Trans Ind Electron 2018;65:6983–93. https://doi.org/10.1109/TIE.2018.2793270.
[10] Fleming TJ, Kavanagh A, Duggan G, O'Mahony B, Higgens M. The effect of induction heating power on the microstructural and physical properties of investment cast ASTM-F75 CoCrMo alloy. J Mater Res Technol 2019;8:4417–24. https://doi.org/10.1016/J.JMRT.2019.07.052.
[11] Fleming TJ, Kavanagh A, Duggan G. The effect of melt temperature on the mechanical properties of cast ASTM F75 CoCrMo alloy as explained by nitrogen and oxygen content. J Mater Res Technol 2020;9:9479–86. https://doi.org/10.1016/J.JMRT.2020.06.079.
[12] Umbrashko A, Baake E, Nacke B, Jakovics A. Modeling of the turbulent flow in induction furnaces. Metall Mater Trans B Process Metall Mater Process Sci 2006;37:831–8. https://doi.org/10.1007/s11663-006-0065-0.
[13] Spitans S, Jakovics A, Baake E, Nacke B. Numerical modeling of free surface dynamics of melt in an alternate electromagnetic field: Part I. Implementation and verification of model. Metall Mater Trans B Process Metall Mater Process Sci 2013;44:593–605. https://doi.org/10.1007/S11663-013-9809-9.
[14] Ščepanskis M, Jakovičs A, Baake E, Nacke B. Solid inclusions in an electromagnetically induced recirculated turbulent flow: simulation and experiment. Int J Multiphas Flow 2014;64:19–27. https://doi.org/10.1016/J.IJMULTIPHASEFLOW.2014.04.004.
[15] Buliński P, Smolka J, Golak S, Przyłucki R, Palacz M, Siwiec G, et al. Numerical and experimental investigation of heat transfer process in electromagnetically driven flow within a vacuum induction furnace. Appl Therm Eng 2017;124:1003–13. https://doi.org/10.1016/J.APPLTHERMALENG.2017.06.099.
[16] Fashu S, Lototskyy M, Davids MW, Pickering L, Linkov V, Tai S, et al. A review on crucibles for induction melting of titanium alloys. Mater Des 2020;186:108295. https://doi.org/10.1016/J.MATDES.2019.108295.
[17] Brown EE, Stulga JE, Jennings L, Salkeld RW. The influence of VIM crucible composition. Vacuum ARC Remelting, and Electroslas Remelting on the Non-Metallic Inclusion Content of MERL 1980;76:159–68.
[18] Sadrnezhaad SK, Raz SB. Interaction between refractory crucible materials and the melted NiTi shape-memory alloy. Metall Mater Trans B 2005;36:395–403.
[19] Gao X yong, Zhang L, hui Qu X, wei Chen X, feng Luan Y. Effect of interaction of refractories with Ni-based superalloy on inclusions during vacuum induction melting. Int J Miner Metall Mater 2020;27:1551–9. https://doi.org/10.1007/s12613-020-2098-9.

[20] Valenza F, Sitzia S, Cacciamani G, Muolo ML, Passerone A, Wojewoda-Budka J, et al. Wetting and interfacial reactivity of Ni–Al alloys with Al2O3 and ZrO2 ceramics. J Mater Sci 2021;56:7849–61. https://doi.org/10.1007/S10853-021-05769-6.

[21] Konrad CH, Brunner M, Kyrgyzbaev K, Völkl R, Glatzel U. Determination of heat transfer coefficient and ceramic mold material parameters for alloy IN738LC investment castings. J Mater Process Technol 2011;211:181–6. https://doi.org/10.1016/J.JMATPROTEC.2010.08.031.

[22] García Ten J, Orts MJ, Saburit A, Silva G. Thermal conductivity of traditional ceramics. Part I: influence of bulk density and firing temperature. Ceram Int 2010;36:1951–9. https://doi.org/10.1016/J.CERAMINT.2010.05.012.

[23] Litovsky E, Gambaryan-Roisman T, Shapiro M, Shavit A. Heat transfer mechanisms governing thermal conductivity of porous ceramic materials. Trends Heat, Mass Momentum Transf 1997;3:147–67.

[24] Vitiello D, Nait-Ali B, Tessier-Doyen N, Tonnesen T, Laím L, Rebouillat L, et al. Thermal conductivity of insulating refractory materials: comparison of steady-state and transient measurement methods. Open Ceram 2021;6:100118. https://doi.org/10.1016/j.oceram.2021.100118.

[25] Schulz B, Hoffmann M. Thermophysical properties of the system Al2O3-MgO. High Temp - High Press 2002;34:203–12. https://doi.org/10.1068/htjr018.

[26] Shi W, Pinto B. Energy savings through thermally efficient crucible technology: fundamentals, process modeling, and applications. JOM 2017;69:2797. https://doi.org/10.1007/s11837-017-2631-0.

[27] Akiyoshi MM, Christoforo AL, Luz AP, Pandolfelli VC. Thermal conductivity modelling based on physical and chemical properties of refractories. Ceram Int 2017;43:4731–45. https://doi.org/10.1016/j.ceramint.2016.11.091.

[28] Sainz MA, Mazzoni AD, Aglietti EF, Caballero A. Thermochemical stability of spinel (MgO·Al2O3) under strong reducing conditions. Mater Chem Phys 2004;86:399–408. https://doi.org/10.1016/J.MATCHEMPHYS.2004.04.007.